



Optics Letters

Cross-polarized, multi-octave supercontinuum generation

HAOCHUAN WANG,^{1,2} AYMAN ALISMAIL,^{2,3} GAIA BARBIERO,² MAXIMILIAN WENDL,² AND HANIEH FATAHI^{1,2,*}

¹Max-Planck Institut für Quantenoptik, Hans-Kopfermann-Str. 1, D-85748 Garching, Germany

²Department für Physik, Ludwig-Maximilians-Universität München, Am Coulombwall 1, D-85748 Garching, Germany

³Physics and Astronomy Department, King Saud University, Riyadh 11451, Saudi Arabia

*Corresponding author: hanieh.fattahi@mpq.mpg.de

Received 5 May 2017; revised 3 June 2017; accepted 7 June 2017; posted 8 June 2017 (Doc. ID 294944); published 29 June 2017

The generation of superoctave spectra from the interaction of intense ultrashort optical pulses and cubic nonlinearity is the result of interplay between the dispersion and nonlinearity of a material and various propagation effects. The cubic nonlinearity can be enhanced when it is combined with a quadratic-cascaded nonlinearity, relaxing the requirement on the laser's peak intensity for supercontinuum (SC) generation. In this Letter, we demonstrate and compare the generation of an SC driven from cubic and cascaded quadratic nonlinearities at an anomalous and zero dispersion wavelength (ZDW). We show the filament-free SC generation of femtosecond mid-infrared pulses by harvesting cascaded quadratic nonlinearity and, at ZDW, requires a lower threshold peak intensity and results in a higher power spectral density for the newly generated spectral components. The presented method is a suitable approach for generating multi-octave spectra from low peak-power, high average-power oscillators or a suitable seed for optical parametric amplifiers and multi-octave field synthesizers. © 2017 Optical Society of America

OCIS codes: (140.0140) Lasers and laser optics; (140.3515) Lasers, frequency doubled; (140.3615) Lasers, ytterbium; (320.2250) Femtosecond phenomena; (320.6629) Supercontinuum generation; (320.7150) Ultrafast spectroscopy.

<https://doi.org/10.1364/OL.42.002595>

Shortly after the invention of lasers, supercontinuum (SC) generation was observed by focusing picosecond pulses into a borosilicate glass [1]. The advancement of high-energy, femtosecond lasers at multi hertz-kilohertz repetition rates led to SC generation in gas, gas-filled hollow-core fibers, and photonic crystal fibers, benefiting chemistry, biology, and condensed matter, and enabling the emergence of new sub-fields such as attophysics [2].

Recent advances in femtosecond spectroscopy toward field-resolved spectroscopy [3–5] demand multi-octave, mid-infrared (MIR) sources at megahertz repetition rates with a carrier-envelope phase (CEP) stability, in order to cover fundamental vibrational absorption bands of many molecules and

solid-state components. Turnkey, Yb:YAG high-power oscillators [6–8] with tens of microjoule pulse energy, when delivering a CEP-stable, multi-octave spectrum, can be extremely attractive sources for pushing biological imaging [9] toward new frontiers such as field-resolved imaging.

SC generation preserves the CEP stability and can extend over several octave spectral components. In SC generation based on cubic nonlinearity, Kerr nonlinearity triggers self-focusing and, consequently, leads to a dramatic spectral broadening [10]. Here, the peak power of the laser should exceed the critical power of self-focusing. To satisfy this condition, the laser pulses have to be focused tightly, which could lead to thermal damage at high average powers due to the high power density. In addition, direct SC generation from Yb:YAG lasers is limited to the visible and near-infrared (NIR) spectral regions, and generating a SC in the MIR spectral range requires several nonlinear stages [11,12] and, consequently, higher pulse energy, beyond the energy level delivered by the current megahertz oscillators.

These limitations can be overcome by employing the quadratic, phase-mismatched cascaded nonlinearity of birefringent media [13] for SC generation. Here, at a strong phase mismatch and large values of ΔkL , a small fraction of the fundamental wave (FW) is converted to the second-harmonic (SH) waves in one coherence length and is converted back to the FW in the next coherence length. The phase shift between the back-converted and unconverted FWs induces a Kerr-like nonlinearity, which is controllable in both magnitude and sign through the phase mismatch value and can result in self-focusing or self-defocusing [14–16]. The cascaded quadratic nonlinearity offers a possibility to reduce the threshold peak intensity of SC generation to below the critical power by increasing the effective nonlinear refractive index [17].

In this Letter, we demonstrate how quadratic-cascaded SC generation in a LiNbO₃ (LNB) crystal pumped at its zero dispersion wavelength (ZDW) can lead to a lower peak intensity threshold for SC generation and a higher power spectral density. We compare this case to quadratic-cascaded SC generation in a beta barium borate (BBO) crystal [18,19] and Kerr-nonlinearity-driven SC in a YAG plate in anomalous dispersion.

We chose BBO and LNB crystals for this Letter, due to their similar structure (trigonal, R3c), but different ZDW (1.4 μm

for BBO and 2 μm for LNB). A quadratic, type I interaction ($o + o \rightarrow e$) with ordinary polarized few-cycle pulses at 2.1 μm as the FWs is considered. In the strongly phase-mismatched regime, in addition to the Kerr nonlinear refractive index (n_2^{Kerr}), a cascaded nonlinear refractive index (n_2^{casc}) is induced to the FWs, which can be calculated from

$$n_2^{\text{casc}} = \frac{4\pi d_{\text{eff}}^2}{\Delta k n_o(2\omega)^2 n_o(\omega)^2 \lambda_0 \epsilon_0 c}, \quad (1)$$

where $\Delta k = k(\lambda_0/2) - 2k(\lambda_0)$, $k = \frac{2\pi n}{\lambda_0}$, and λ_0 , ϵ_0 , n_o , respectively, are the central wavelength, vacuum permittivity, and ordinary refractive index of the nonlinear medium. The effective nonlinear index, n_2^{eff} , is the sum of the n_2^{casc} and the n_2^{Kerr} . The input parameters for the following estimations are summarized in Table 1.

Figure 1 compares the dispersion and the induced nonlinear phase shift for both crystals at a 2 mm thickness. As can be seen in panel (a), for 2.1 μm pulses, the phase mismatch becomes zero at $\theta = 45.05^\circ$ and $\theta = 21.5^\circ$ for LNB and BBO, respectively.

The group velocity dispersion (GVD) for the BBO crystal at 24.7° is $-157.0298 \text{ fs}^2/\text{m}$, and the phase mismatch is -58.44 , giving rise to an effective cascaded positive Kerr nonlinearity. At this angle, the induced cascaded quadratic nonlinearity is in the self-focusing regime and is larger than the cubic nonlinearity of the crystal. In fact, we have $n_2^{\text{casc}} = 8.92 \times 10^{-16} \text{ cm}^2/\text{W}$, $n_2^{\text{Kerr}} = 5.61 \times 10^{-16} \text{ cm}^2/\text{W}$. This regime allows for solitary wave dynamics where the pulse undergoes a strong compression due to high-order cubic soliton excitation and the generation of linear dispersive waves in the blue spectral components [22].

However, for LNB at 45.85° , the GVD and the phase mismatch are $-74.8813 \text{ fs}^2/\text{m}$ and -12.28 , respectively. Due to a larger d_{eff} of LNB, the cascaded nonlinearity and the cubic nonlinearity values are much bigger than for BBO: $n_2^{\text{casc}} = 90.3 \times 10^{-16} \text{ cm}^2/\text{W}$ and $n_2^{\text{Kerr}} = 20.7 \times 10^{-16} \text{ cm}^2/\text{W}$. In addition, the lower GVD in LNB allows for longer propagation of few-cycle pulses with a negligible decrease in their peak intensity.

These two regimes of quadratic SC generation were investigated by using few-cycle, CEP stable pulses at 2.1 μm [12] generated directly from a Yb:YAG thin-disk amplifier [23] to pump a BBO and LNB crystal at an anomalous and ZDW, respectively. The crystals were mounted on a rotational and translational stage, first, to allow varying the angle of the incident beam relative to the optical axis of the crystal in the phase-matching plane for second-harmonic generation (SHG) and, secondly, to adjust the peak intensity of pulses by scanning through the focus in order to change the pulse's beam size.

Table 1. Parameters Used for the Calculation of the Effective Nonlinear Indices of Different Crystals

Crystal	λ (μm)	Nonlinear Coefficients	
		(pm/V)	$n_2^{\text{Kerr}} \times 10^{-16} (\text{cm}^2/\text{W})$
YAG	2.1	Isotropic	6.9
BBO	2.1	$d_{22} = 2.2/d_{31} = 0.04$	<i>o</i> -axis = 5.61,
			<i>e</i> -axis = 2.34 [20]
LNB	2.1	$d_{22} = 2.6/d_{31} = 4.6$	<i>o</i> -axis = 20.7,
			<i>e</i> -axis = 16.5 [21]

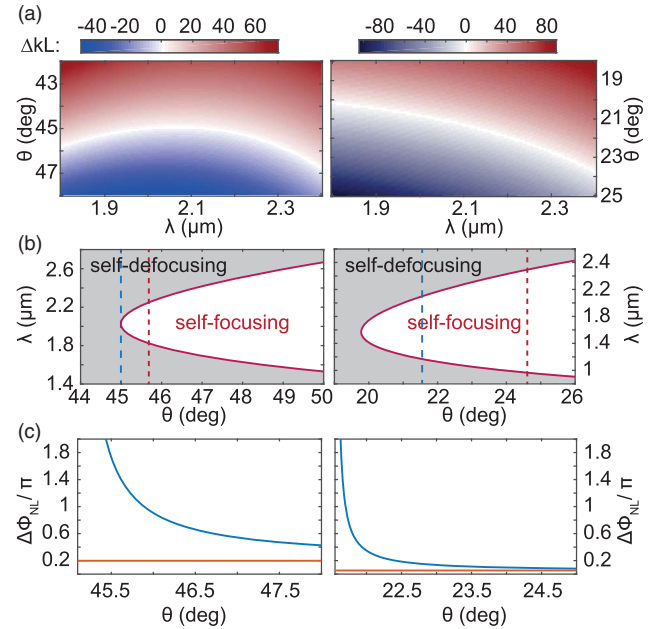


Fig. 1. Calculated ΔkL for a 2 mm thick LNB crystal (left) and a 2 mm thick BBO crystal (right) versus a wavelength and phase-matching angle of each crystal (a). Type I phase-matching curves for LNB (left) and BBO (right). The blue dashed line shows the phase-matching angle for second-harmonic generation, and the red dashed line shows the angle of operation for continuum generation. The gray shaded area shows n_2^{casc} with negative values (b). Calculated nonlinear phase shift for a 2 mm thick LNB (left) and 2 mm thick BBO (right) crystal. The red line shows the phase shift due to the Kerr nonlinearity (c).

To study the SC generation in anomalous dispersion, 2 μJ energy of 2.1 μm pulses were focused by using a $f = 75 \text{ mm}$ convex CaF_2 lens and sent to a 2 mm thick, type I BBO crystal. The polarization of the input pulses was set parallel to the ordinary axis of the crystal, and the phase-matching angle of the crystal was scanned to achieve a SC with a broadest spectral bandwidth and best spatial profile.

Figure 2(a) shows the broadest generated spectrum and its corresponding spatial intensity profile. The polarization of the SC was analyzed by measuring the spectrum behind a broadband polarizer in ordinary and extraordinary polarization, as shown in Figs. 2(b) and 2(c). Due to the induced negative ΔkL at 24.7° , the effective nonlinear index is increased. In this regime, the required power for generating a SC is below the critical power for self-focusing.

The spatial intensity profile of the SC was measured for both polarizations with a silicon charge-coupled device camera (Dataray Wincam), making use of the two-photon absorption in silicon for detection of the spatial profile of the FW (Fig. 2 insets). The portion of the SC with an ordinary polarization has a Gaussian spatial profile and follows the properties of SC generation based on cubic nonlinearity. However, on extraordinary polarization, the spatial profile has a complex structure [24]. The generated spectrum on this axis is associated to the collinear SH phase matching of certain spectral components of the generated SC on the ordinary axis [17]. The red dashed line in Fig. 1(b) indicates two resonances at 2.4 μm and at 900 nm.

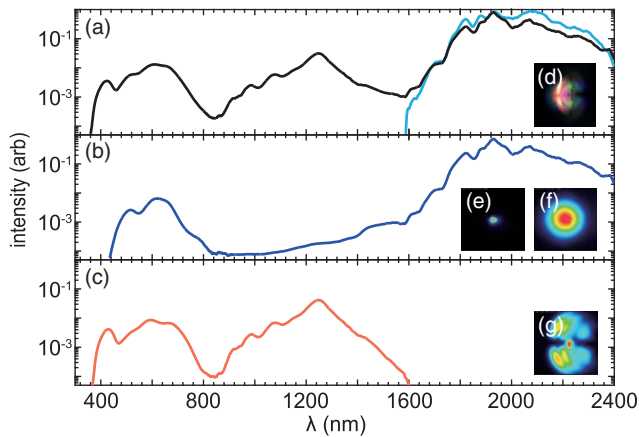


Fig. 2. Spectral intensity of the fundamental (blue curve) and the generated SC (black curve) in a 2 mm thick BBO crystal (a). The portion of the spectrum with (b) ordinary and (c) extraordinary polarization. Insets: the picture of generated white light (d) and the transverse spatial intensity profile of the shown spectra for spectral components below $1 \mu\text{m}$ in (e) the far field and (f, g) the near-field.

The effect of these two resonances in SC generation via SHG can be seen on the extraordinary polarized spectrum of the SC with two peaks around $1.2 \mu\text{m}$ and 500 nm .

For SC generation at ZDW, the same pulses were sent into a 2 mm thick, type I LNB crystal. The broadest spectrum with a good spatial profile, spanning from 800 to beyond 2400 nm [Fig. 3(a)] is generated at $\theta = 45.85^\circ$. Figures 3(b) and 3(c) show portions of the SC with ordinary and extraordinary polarizations and their corresponding spatial intensity profile. Here, unlike for BBO, the spatial profile of the FW is imprinted on the spatial profile of the newly generated frequencies with ordinary and extraordinary polarizations.

Due to the high effective nonlinear refractive index, the fundamental spectrum at ordinary polarization is broadened to

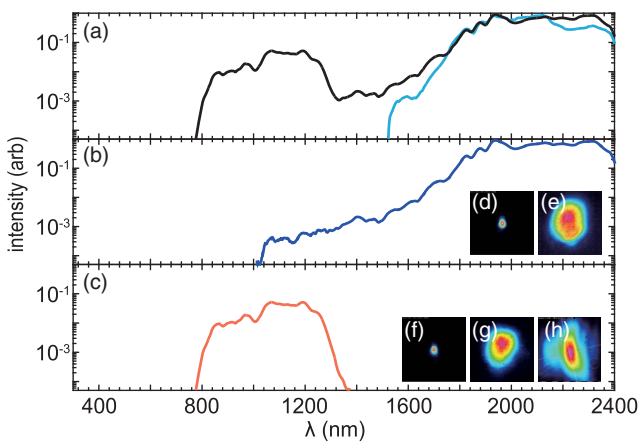


Fig. 3. Spectral intensity of the fundamental (blue curve) and the generated SC (black curve) in a 2 mm thick LNB crystal (a). The portion of the spectrum with (b) ordinary and (c) extraordinary polarization. Insets: the transverse spatial intensity profile of the shown spectra for spectral components above $1 \mu\text{m}$ in (d) the far field and (e) the near field, and below $1 \mu\text{m}$ in the focusing regime in (f) the far field and (g) the near field, and (h) the defocusing regimes in the near field.

beyond $2.4 \mu\text{m}$. Simultaneously, due to the high intensity of the FW in the crystal, broadband SH pulses with an extraordinary polarization, spanning 900 nm to $1.1 \mu\text{m}$, are generated. This bandwidth is defined by the two resonance points at 1.8 and $2.2 \mu\text{m}$ [the intersection of the red dashed line and the red solid line in Fig. 1(b)]. At $16 \text{ GW}/\text{cm}^2$ and 45.05° , the SHG efficiency is 6% , which drops to 0.2% at 45.85° with a similar spectral bandwidth. By increasing the peak intensity, four-wave mixing and, mainly $o+e+o \rightarrow e$ and $e+e+e \rightarrow e$ interactions, sets in and spectrally broadens the FWs and SH waves. As the coherence length of the generated SH is $2/\Delta k = 325.7 \mu\text{m}$, the Kerr-based broadening of the pulses with extraordinary polarization happens just at the last half a millimeter of the crystal.

We observed similar spectral broadening in a self-defocusing regime by changing the phase-mismatching angle of the LNB crystal to 44.25° . However, in this regime, higher peak intensity is required to generate the SC, and the spatial profile of the extraordinary polarized components of the SC becomes distorted [see Fig. 3(f)].

The temporal profile of the MIR portion of the SC in LNB was characterized by using a frequency-resolved optical gating device based on second-harmonic generation (SH-FROG) containing a $100 \mu\text{m}$ thick BBO crystal. The dominant contribution of SHG in SC can be seen by comparing the retrieved spectrum of the SC in the MIR range and the spectrum of the FWs in Fig. 4(a). The induced phase due to SC generation shown in Fig. 4(a) (black dotted line) is calculated by subtracting the spectral phase of the FWs after SC generation from the spectral phase of the input pulses. As the intensity of the newly generated frequencies with extraordinary polarization is relatively low, we chose to amplify their energy in an optical parametric amplifier similar to [25], before characterizing their spectral phase by a SH-FROG containing a $10 \mu\text{m}$ thick BBO crystal. The amplifier includes a 15 mm thick fused silica stretcher. Figure 4(b) shows the retrieved spectral intensity of the amplified pulses in an NIR spectral range and its corresponding spectral phase.

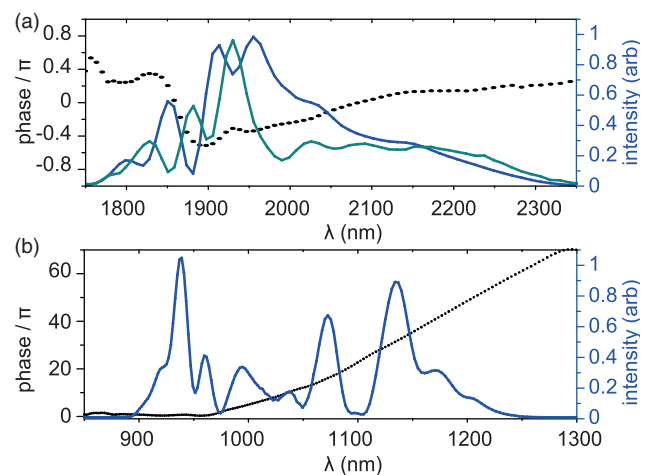


Fig. 4. Retrieved spectral intensity of the fundamental (blue curve) and SC pulses after a 2 mm thick LNB crystal (cyan) measured by SH-FROG. The black curve shows the induced spectral phase on the FWs by SC generation (a). Retrieved spectral intensity (blue curve) and spectral phase (black curve) of the amplified portion of the generated SC in the NIR spectral range (b).

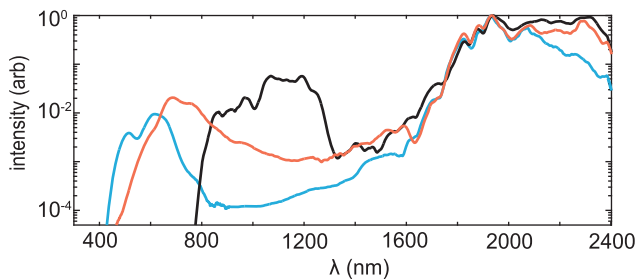


Fig. 5. Comparison between the generated SC in the 2 mm thick YAG (red), LNB (black), and the ordinary polarization of the BBO crystal (blue). Each spectrum is normalized to one.

In conclusion, by harvesting the quadratic-cascaded nonlinearity in birefringent nonlinear media at ZDW, a SC with a good temporal and spatial profile can be generated. We observed the polarization rotation in the visible spectral range of the generated continuum relative to the polarization of the FWs.

The polarization rotation originates from SHG; as for high peak intensities, Kerr nonlinearities set in and give rise to a nonlinear phase mismatch and to self- and cross-action of the interacting FW and SH pulses, leading to their spectral broadening [22]. We observed a higher SC cutoff in BBO due to its higher bandgap and different dynamic in the anomalous dispersion [26]. However, the spatial profile of the extraordinary polarized spectral components in BBO is complex. The temporal analysis of the MIR and NIR spectral components of the generated SC in LNB shows a well-behaved spectral phase and an excellent coherence.

Figure 5 compares SC generation in LNB and BBO with a 2 mm thick YAG plate under the same initial conditions, except for the beam size in the nonlinear medium. As can be seen, the power spectral density of the newly generated frequencies in LNB is enhanced. Additionally, in comparison to BBO and YAG, the required critical power for SC generation in LNB in the self-focusing regime is lower by more than one order of magnitude. The SC process in ZDW is fuelled by different processes below and above the ZDW, such as cascading-induced self-focusing, self-steepening soliton and dispersive wave formation.

The polarization rotation of the generated SC in LNB can be avoided by using a type 0 phase matching, when it is demanded. In addition, the bandwidth of the cascaded nonlinearity can be engineered and optimized by using periodically poled structures.

Quadratic SC generation at ZDW has two prominent applications. The possibility of increasing the effective nonlinear refractive index in a nonlinear medium allows for SC generation at lower peak intensities. Therefore, SC can be generated at a looser focusing condition with a lower power density, offering a new route for Watt-level SC generation. Here, a SC can be generated at a lower power density compared to the SC generation based on cubic nonlinearity, which allows for scaling the input average power. Additionally, the generated spectrum can serve as a seed for broadband optical parametric amplifiers and field synthesizers [27]. Specifically, for seeding the new generation of high-energy, sub-cycle light transients based on cross-polarized wave synthesis [28].

Funding. Centre for Advanced Laser Applications (CALA).

Acknowledgment. The authors wish to thank Ferenc Krausz for his support.

REFERENCES

1. R. R. Alfano and S. L. Shapiro, *Phys. Rev. Lett.* **24**, 584 (1970).
2. F. Krausz and M. Ivanov, *Rev. Mod. Phys.* **81**, 163 (2009).
3. S. Keiber, S. Sederberg, A. Schwarz, M. Trubetskov, V. Pervak, F. Krausz, and N. Karpowicz, *Nat. Photonics* **10**, 159 (2016).
4. C. Riek, D. V. Seletskiy, A. S. Moskalenko, J. F. Schmidt, P. Krauspe, S. Eckart, S. Eggert, G. Burkard, and A. Leitenstorfer, *Science* **350**, 420 (2015).
5. M. Eisele, T. L. Cocker, M. A. Huber, M. Plankl, L. Viti, D. Ercolani, L. Sorba, M. S. Vitiello, and R. Huber, *Nat. Photonics* **8**, 841 (2014).
6. O. Pronin, M. Seidel, F. Lücking, J. Brons, E. Fedulova, M. Trubetskov, V. Pervak, A. Apolonski, T. Udem, and F. Krausz, *Nat. Commun.* **6**, 6988 (2015).
7. S. Hädrich, M. Kienel, M. Müller, A. Klenke, J. Rothhardt, R. Klas, T. Gottschall, T. Eidam, A. Drozdy, P. Jójárt, Z. Várallyay, E. Cormier, K. Osvay, A. Tünnermann, and J. Limpert, *Opt. Lett.* **41**, 4332 (2016).
8. C. J. Saraceno, F. Emaury, C. Schriber, M. Hoffmann, M. Golling, T. Südmeyer, and U. Keller, *Opt. Lett.* **39**, 9 (2014).
9. J.-X. Cheng and X. S. Xie, *Science* **350**, aaa8870 (2015).
10. F. Silva, D. R. Austin, A. Thai, M. Baudisch, M. Hemmer, D. Faccio, A. Couairon, and J. Biegert, *Nat. Commun.* **3**, 807 (2012).
11. I. Pupeza, D. Sánchez, J. Zhang, N. Lilienfein, M. Seidel, N. Karpowicz, T. Paasch-Colberg, I. Znakovskaya, M. Pescher, W. Schweinberger, V. Pervak, E. Fill, O. Pronin, Z. Wei, F. Krausz, A. Apolonski, and J. Biegert, *Nat. Photonics* **9**, 721 (2015).
12. H. Fattahi, H. Wang, A. Alismail, G. Arisholm, V. Pervak, A. M. Azzeer, and F. Krausz, *Opt. Express* **24**, 24337 (2016).
13. B. B. Zhou, A. Chong, F. W. Wise, and M. Bache, *Phys. Rev. Lett.* **109**, 4499 (2012).
14. K. Krupa, A. Labruyère, A. Tonello, B. M. Shalaby, V. Couderc, F. Baronio, and A. B. Aceves, *Optica* **2**, 1058 (2015).
15. R. Šuminas, G. Tamošauskas, V. Jukna, A. Couairon, and A. Dubietis, *Opt. Express* **25**, 6746 (2017).
16. K. Beckwitt, F. W. Wise, L. Qian, L. A. Walker, and E. Canto-Said, *Opt. Lett.* **26**, 1696 (2001).
17. R. Šuminas, G. Tamošauskas, G. Valiulis, and A. Dubietis, *Opt. Lett.* **41**, 2097 (2016).
18. B. Zhou, H. Guo, and M. Bache, *Opt. Express* **23**, 6924 (2015).
19. B. Zhou and M. Bache, *Opt. Lett.* **40**, 4257 (2015).
20. R. Ganeev, I. Kulagin, A. Rysnyansky, R. Tugushev, and T. Usmanov, *Opt. Commun.* **229**, 403 (2004).
21. R. A. Ganeev, I. A. Kulagin, A. I. Rysnyansky, R. I. Tugushev, and T. Usmanov, *Opt. Spectrosc.* **94**, 561 (2003).
22. M. Conforti and F. Baronio, *J. Opt. Soc. Am. B* **30**, 1041 (2013).
23. H. Fattahi, A. Alismail, H. Wang, J. Brons, O. Pronin, T. Buberl, L. Vámos, G. Arisholm, A. M. Azzeer, and F. Krausz, *Opt. Lett.* **41**, 1126 (2016).
24. D. Majus, G. Tamošauskas, I. Gražulevičiūtė, N. Garejev, A. Lotti, A. Couairon, D. Faccio, and A. Dubietis, *Phys. Rev. Lett.* **112**, 193901 (2014).
25. A. Alismail, H. Wang, A. M. Azzeer, F. Krausz, and H. Fattahi, *Lasers and Electro-Optics Europe (CLEO EUROPE/IQEC), 2013 Conference on and International Quantum Electronics Conference (IEEE)*, (2017).
26. A. Brodeur and S. L. Chin, *Phys. Rev. Lett.* **80**, 4406 (1998).
27. H. Fattahi, H. G. Barros, M. Gorjan, T. Nubbemeyer, B. Alsaif, C. Y. Teisset, M. Schultze, S. Prinz, M. Haefner, M. Ueffing, A. Alismail, L. Vámos, A. Schwarz, O. Pronin, J. Brons, X. T. Geng, G. Arisholm, M. Ciappina, V. S. Yakovlev, D.-E. Kim, A. M. Azzeer, N. Karpowicz, D. Sutter, Z. Major, T. Metzger, and F. Krausz, *Optica* **1**, 45 (2014).
28. H. Wang, A. Alismail, F. Krausz, and H. Fattahi, in *Lasers and Electro-Optics Europe (CLEO EUROPE/IQEC), 2013 Conference on and International Quantum Electronics Conference (IEEE)*, (2017).